

Solar magnetic elements at 0".1 resolution

II. Dynamical evolution

L. H. M. Rouppe van der Voort^{1,2}, V. H. Hansteen^{1,2}, M. Carlsson^{1,2}, A. Fossum¹, E. Marthinussen¹,
M. J. van Noort^{1,2}, and T. E. Berger³

¹ Institute of Theoretical Astrophysics, University of Oslo, PO Box 1029 Blindern, 0315 Oslo, Norway
e-mail: rouppe@astro.uio.no

² Center of Mathematics for Applications, University of Oslo, PO Box 1053 Blindern, 0316 Oslo, Norway

³ Lockheed Martin Solar and Astrophysics Lab, 3251 Hanover St., Palo Alto, California, 94304, USA

Received 17 December 2004 / Accepted 28 January 2005

Abstract. Small magnetic structures can be seen in *G*-band filtergrams as isolated bright points, strings of bright points and dark micro-pores. At a resolution of 0".1, new forms of magnetic structures are found in strong field areas: elongated “ribbons” and more circular “flowers”. In this paper we study the temporal evolution of these small scale magnetic structures. In strong-field regions the time-evolution is more that of a magnetic fluid than that of collections of flux-tubes that keep their identity. We find that the granular flow concentrates the magnetic field into flux sheets that are visible as thin bright features in the filtergrams. Weak upflows are found in the flux sheets and downflows in the immediate surroundings. The flux sheets often become unstable to a fluting instability and the edges buckle. The sheets tend to break up into strings of bright points, still with weak upflows in the magnetic elements and zero velocity or downflows between them. Where there are larger flux concentrations we find ribbons, flowers and micro-pores. There is a continuous transition between these forms and they evolve from one form to another. The appearance is mostly determined by the horizontal size – larger structures are dark (micro-pores), narrower structures are ribbon shaped and the flowers are the smallest in extent. All these structures have darker inner parts and a bright edge. The plasma is found to be at rest in the ribbons, with small concentrations of weak upflow sites. Narrow sheets with downdrafts are found right at the edges of the magnetic field concentrations.

Key words. Sun: faculae, plages – Sun: magnetic fields – Sun: granulation – Sun: photosphere

1. Introduction

Convective flows play a major role in the dynamical evolution of small-scale magnetic field structures. In quiet areas where magnetic field concentrations appear as isolated bright points, the lateral motions are totally dominated by the granular flows. These isolated bright points appear to be passively advected towards the periphery of supergranular cells (Muller 1983) where they gather and form the magnetic network. In stronger field areas, like in active region plage or enhanced network, magnetic structures behave less passively and seem to affect the granular flow. Granules near network bright points are smaller, have lower contrast and display slower temporal behavior (Dunn & Zirker 1973; Title et al. 1992). The granular pattern in these magnetically dominated areas are referred to as “abnormal”.

Several studies of the statistical properties of the dynamical evolution of bright points have appeared in the literature. Berger & Title (1996) described a number of evolutionary effects during the lifetime of bright points. These include shape modifications such as elongation, rotation, folding, splitting and merging. Significant morphological changes can occur on

time scales as short as 100 s and are strongly dependent on the local granular convective flow field. These changes make it difficult to define a typical lifetime of bright points. Berger et al. (1998) found an average lifetime of 9.3 min using automated feature tracking techniques on a 70 min sequence of enhanced magnetic network. Some bright points persist up to the entire 70 min, and they experience numerous merging and splitting events but are still regarded as single objects. In a study of isolated bright points in a network region, Nisenson et al. (2003) found a similar mean lifetime of 9.2 min with the longest-lived bright point lasting 25 min. These reported values for the mean lifetime are very similar to the evolution time scale of granulation.

Berger et al. (1998) concluded that most of the time bright points follow the granular flow fields: they found very similar values (about 300 m s⁻¹) for the modal speed of their measurements of bright point and flow field velocities. The bright point velocity distribution differed markedly for higher velocities by possessing a significant high speed tail with velocities up to 4 km s⁻¹. Their reported value for the mean speed of 1.47 km s⁻¹ compares well with the values reported by

Berger & Title (1996): $1\text{--}2\text{ km s}^{-1}$ and Muller et al. (1994): 1.33 km s^{-1} but is higher than the values reported by Nisenson et al. (2003): 0.89 km s^{-1} and Bovelet & Wiehr (2003): 0.85 km s^{-1} .

The predominant shape of isolated bright points is circular, Berger et al. (1995) found that 60% of the bright points in their sample are circular with an average eccentricity of 1.5. Bovelet & Wiehr (2003) found a similar fraction of 67% of circular bright points. Both studies found similar values for the most frequent bright point diameter in their samples: 220 km. The sharp cut-off in the size distributions at sizes near the telescope diffraction limit indicates that many bright points were unresolved and smaller bright points might exist. This implied that larger, extended magnetic regions, such as the low-contrast amorphous features reported in Berger et al. (1995), could consist of conglomerates of unresolved bright points. Similarly, narrow bands of enhanced brightness could consist of strings of unresolved bright points in close proximity.

With the commissioning of the Swedish 1-m Solar Telescope (Scharmer et al. 2003a, SST), solar observations at a resolution of 0'.1 have become available – improving the spatial resolution by about a factor 2. Berger et al. (2004, Paper I) used the SST to obtain a set of excellent cotemporal images taken in different passbands of remnant active region plage. At a resolution of 0'.1, new forms of magnetic structures are found in the strong field areas.

Besides being scattered into isolated flux tubes like in quiet areas, magnetic flux is also found to be structured into larger, amorphous, “ribbons” in the plage regions that contain high net flux. Larger flux concentrations are found as diverging ribbons having maximum brightness on the sides with an intensity depression in the center. Circular manifestations of these spread-out ribbon structures, of which many examples were found, are dubbed “flowers”. The “flowers” and diverging ribbons have typical scales smaller than 1", larger flux concentrations are embedded in (micro-)pores with a distinct dark center. Notable are the “translucent” micropores which reveal convection structures “underneath” the central darkened region. These forms of micropores have also been seen in previous SST observations of active regions (Scharmer et al. 2002, 2003c).

From studying these single images and comparing these different small-scale magnetic structures in strong field areas, it seemed likely that ribbons, “flowers” and micropores are dynamically related in the sense that one structure may evolve into another depending on the amount of magnetic flux that is collected or dispersed. Indeed, from studying image sequences like the ones presented in this paper, we see that ribbons diverge, turn into flowers, become micropores and evolve back again.

Bright points and faculae are bright since they mark regions where the magnetic field is sufficiently high to force evacuation of the gas contained in the magnetic region. This implies that the location where $\tau = 1$ is moved further down into the Sun and thus that the observer samples regions geometrically below the general quiet photosphere. With the temperature increasing with depth one may thus sample a higher temperature in the magnetic flux concentration than outside even if the temperature at a given geometric height is lower

inside than outside (because of the lack of convective energy transport in the magnetic flux concentration). In the *G*-band the contrast is enhanced because of higher formation height due to the many spectral lines (mainly from CH) in the passband and a steeper temperature gradient around $\tau = 1$ in the granules than in the magnetic flux concentration and because of a larger height difference because of CH destruction at low densities. For a discussion of why *G*-band bright points are bright, see Kiselman et al. (2001); Rutten et al. (2001); Sánchez Almeida et al. (2001); Steiner et al. (2001); Schüssler et al. (2003); Uitenbroek (2003); Carlsson et al. (2004); Shelyag et al. (2004)

As described above, a number of magnetic phenomena were presented for the first time as observed with 0'.1 spatial resolution in Paper I. In this paper we return to several of these phenomena and describe their temporal evolution during the course of 86 min.

2. Observations

2.1. Instrumentation

The observations were obtained with the Swedish 1-m Solar Telescope (SST, Scharmer et al. 2003a) on La Palma. Details of the optical setup and instrumentation are described in Paper I, below we briefly summarize the most important aspects of the observations.

Narrow-band interference filters were used for quasi-simultaneous imaging in the line core of the Ca II H line (396.9 nm, filter passband 0.3 nm), the *G*-band (430.5 nm) and near-by continuum (436.4 nm, *G*-cont). The Solar Optical Universal Polarimeter (SOUP, Title & Rosenberg 1981) was used to obtain magnetograms and Dopplergrams in the Ni I 676.8 nm line.

Seeing effects were reduced using several complementary techniques: adaptive optics (AO, Scharmer et al. 2003b) utilizing both a tip-tilt mirror and a deformable mirror, real-time frame selection, and post-processing using the Multi Frame Blind Deconvolution (MFBD) image reconstruction technique (Löfdahl 2002, Appendix A of Paper I).

2.2. Observing program

In this paper we concentrate on a 1.5 h time series obtained on 2 June 2003 during excellent seeing conditions. We observed active region (AR) 10373 at heliographic coordinates N6.1, E5.7 ($\mu = 0.99$) with the field of view (FOV) centered on the large (leading) pore, see Fig. 1. This pore had the same (positive) magnetic polarity as the dominating sunspot which was positioned with one quarter of its surface area in one of the corners of the FOV. A large fraction of the total area is covered with active region plage of mainly positive magnetic polarity.

The time series started at 8:27:54 UT and during 86 min, the seeing conditions remained stable with only a few brief moments of lower quality. After the data processing described below, the resulting co-temporal data sequences are of consistent high quality.

The three science cameras for Ca II H, *G*-band and *G*-cont operated with a frame selection interval of 15 s during which

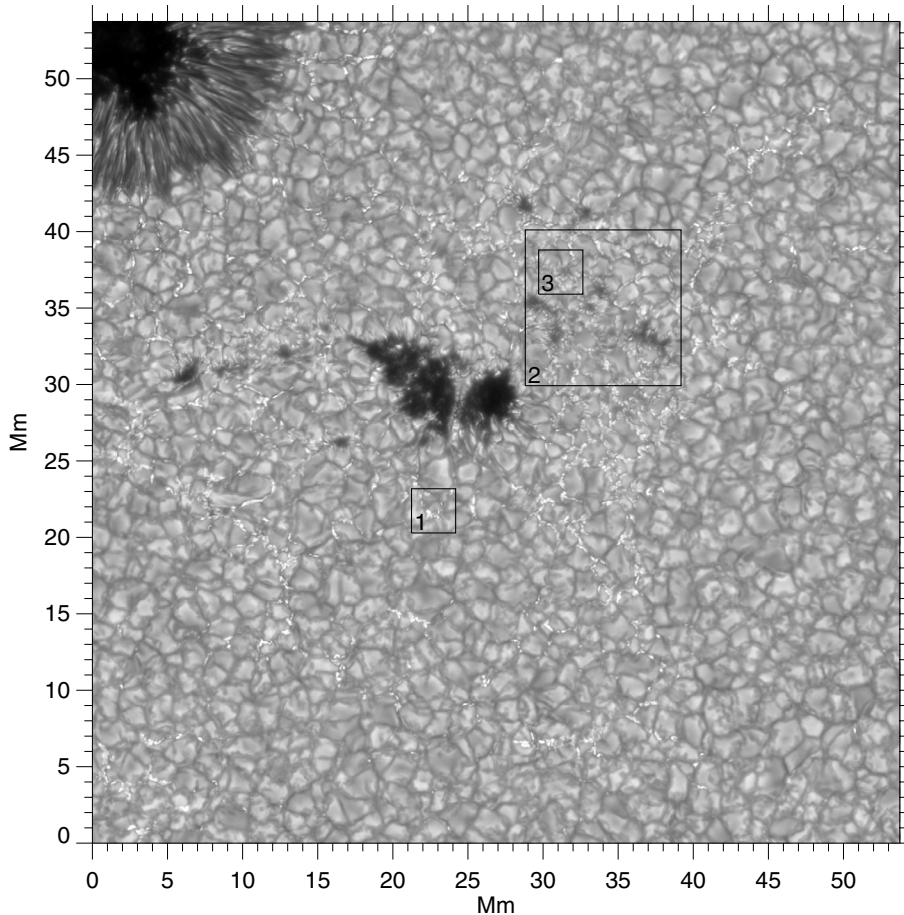


Fig. 1. *G*-band 430.5 nm filtergram of AR 10373. Regions-of-interest 1–3 are marked.

3 images with the highest sharpness values were selected. Including overhead time for data storage, the final *G*-band sequence has a mean cadence of 19.3 s and comprises 268 images. The common FOV for these 3 channels is $74''.2 \times 75''.5$ ($0''.041 \text{ pixel}^{-1}$).

The SOUP instrument was running a sequence emulating the SOHO/MDI observing mode for constructing Dopplergrams and magnetograms. Right and left circular polarization (RCP and LCP) image pairs were taken at 4 different positions through the Ni I 676.8 nm line, separated by 7.5 pm, starting in the blue wing at 11.2 pm from the line core. For each line position and polarization state, 3 images were selected during a frame selection interval of 5 s. The total time for a complete cycle through all 4 line positions was about 1 min. The SOUP images have different dimensions and plate scale ($0''.064 \text{ pixel}^{-1}$) than the other three channels resulting in a common FOV of $74''.2 \times 66''$.

3. Data reduction

After the standard flat field and dark current corrections, all the frame-selected image triplets were used to produce single, reconstructed images with the MFBD technique (see Paper I and Löfdahl 2002). Given the good seeing conditions, the MFBD processing produced excellent results for almost all the images. A few images suffer from artifacts in the form of enhanced

contrast and localized, high-frequency intensity modulations. These artifacts stem from overcompensation for higher order aberrations and illustrate the limitations of the MFBD technique on lower quality data.

The MFBD processed images were aligned by cross-correlation and corrected for the diurnal field rotation, for the *G*-band resulting in an image “cube” of 268 frames. Seeing-induced image warping (caused by anisoplanatism) was removed by destretching the images by iterative cross-correlation of sub-images down to $2''.6 \times 2''.6$ in size. Brightness oscillation from the 5-min *p*-modes were attenuated by using a subsonic Fourier filter (Title et al. 1989) which removes modulations with horizontal speeds above a certain threshold. For the *G*-band and *G*-cont, 4 km s^{-1} was used as the threshold speed, for Ca II H a higher threshold of 7 km s^{-1} was needed in order to not to affect the shorter chromospheric evolution time scale in the data. Besides removing much of the *p*-mode power, a substantial amount of temporal noise is removed, which stems from residual differential image motion.

The *G*-band data cube was used as reference to which all other images were aligned. This was done following the procedure described in Paper I, selecting the closest Ca II H and *G*-cont images to each *G*-band frame.

The total time of the stepping cycle on SOUP was too long ($\approx 1 \text{ min}$) to produce reliable high-resolution magnetograms and Dopplergrams. Therefore, only the exposures in the inner

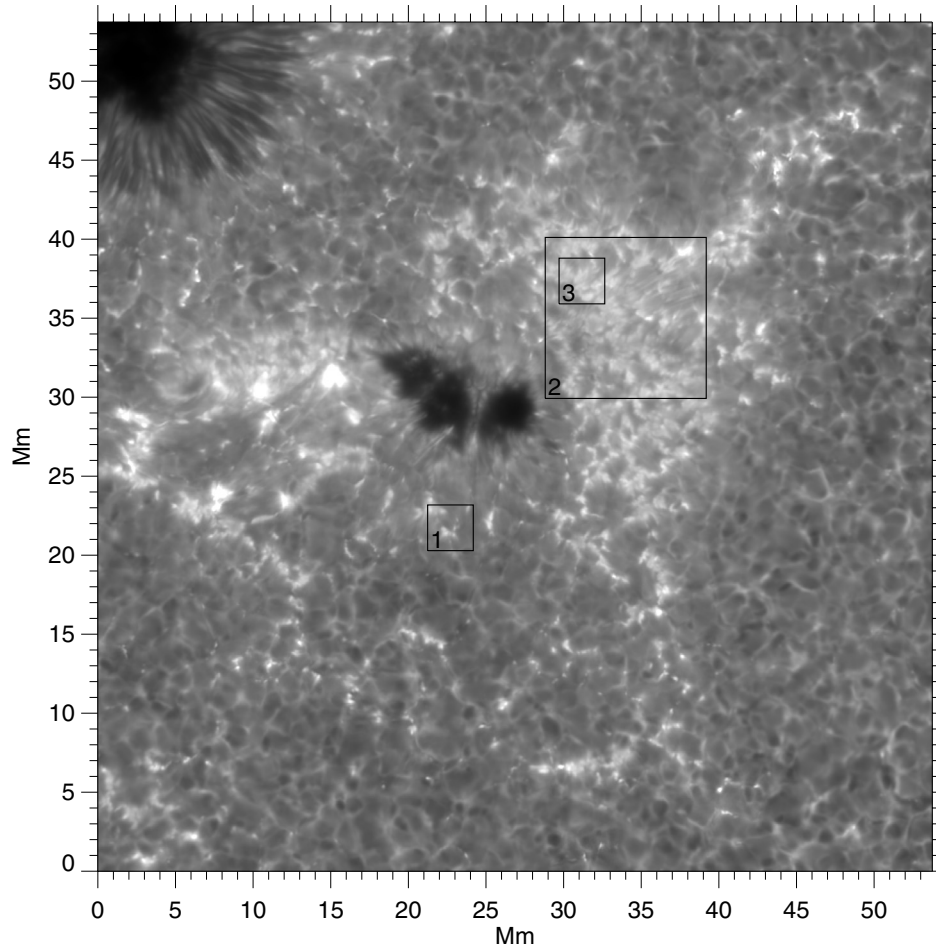


Fig. 2. Ca II H 396.9 nm filtergram of AR 10373.

wing of the Ni I line were taken in order to minimize spurious signals due to solar evolution. Ni I magnetograms were constructed from -3.7 pm LCP and RCP images following the procedure discussed in Appendix B of Paper I. The average time between the LCP and RCP images was 6.7 s. The procedure for the Ni I Dopplergrams differs from the one used in Paper I where only the -3.7 pm and $+3.7$ pm RCP images were used. For this study, the Dopplergrams were made by averaging an RCP Dopplergram made from -3.7 pm and $+3.7$ pm RCP images and an LCP Dopplergram from -3.7 pm and $+3.7$ pm LCP images. The average time between the RCP images was 7.4 s, and between the LCP images 21.2 s. This method reduces the effect of magnetic fields on the Doppler measurements at the expense of a slight reduction of spatial resolution by including more images taken during a longer time period.

Before constructing the magnetograms and Dopplergrams, the images for each polarization state and line position were treated as separate image sequences applying de-rotation, alignment, destretching and subsonic Fourier filtering (with a threshold of 4 km s^{-1}). The LCP and RCP pairs in both line positions were co-aligned using destretching to minimize seeing-induced local offsets. Local cross-correlation between images in the two opposite line wings was impossible since the images differ too much so only global offsets could be removed when constructing Dopplergrams.

The calibrations were done using high-resolution SOHO/MDI magnetograms and Dopplergrams following the procedures discussed in Paper I. The level of accuracy of the calibrated Dopplergrams is estimated to be about 150 m s^{-1} . The sensitivity level of the magnetograms is of the same order as the Fe I 630.2 nm magnetogram discussed in Paper I: about 130 Mx cm^{-2} .

Co-alignment of the magnetograms to the other datasets was done using parameters determined from alignment of the -3.7 pm RCP images to the *G*-band. For the Dopplergrams, the sum of $+3.7$ pm RCP and LCP images were used to co-align to the *G*-band. The cadence for the magnetogram and Dopplergram data cubes is lower than for the *G*-band data: 61.5 s (84 frames).

4. Description and analysis

The full FOV of the observations (see Figs. 1–4) contains examples of solar magnetic structures over a large range of spatial scales: isolated bright points in the more quiet regions, amalgamations of bright points or filigree in the plage areas, pores of different sizes including a large pore with a light bridge and rudimentary penumbra and finally (part of) a sunspot. In the following we concentrate on the dynamical evolution of the smallest magnetic structures. First we give a general

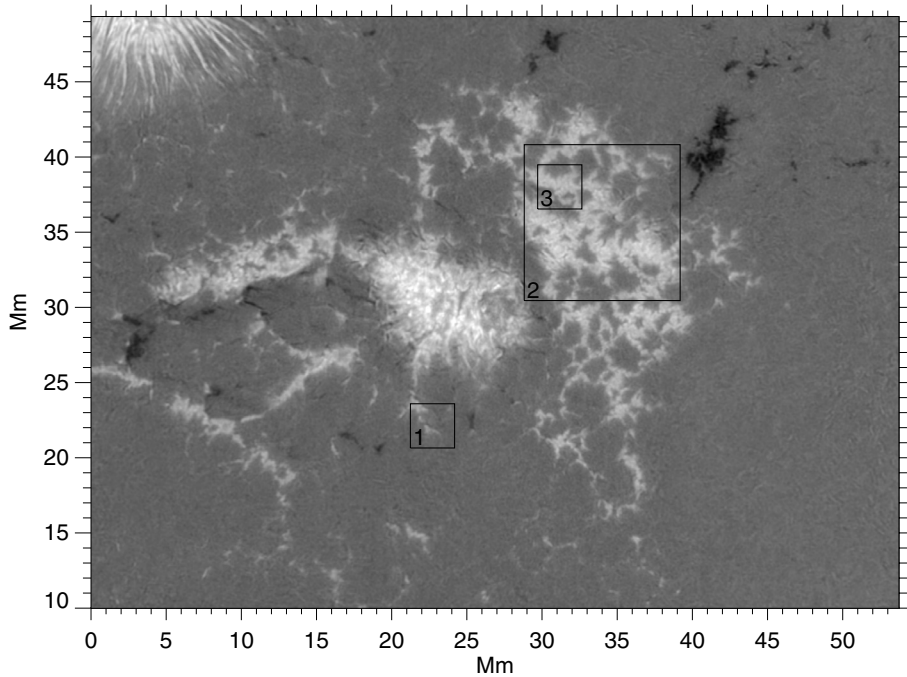


Fig. 3. Ni I 676.8 nm magnetogram of AR 10373. The contrast is a linear scaling of magnetic flux density from -1500 to 1500 Mx cm^{-2} .

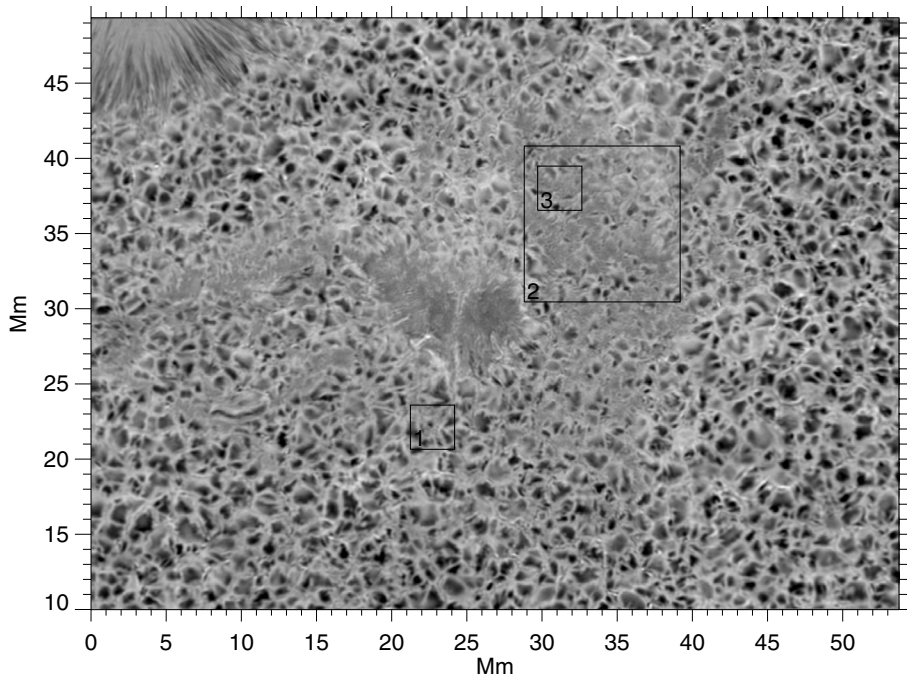


Fig. 4. Ni I 676.8 nm Dopplergram of AR 10373. The contrast is a linear scaling of Dopplershift from -1000 to 1000 m s^{-1} with positive values corresponding to downward velocity and white in the figure.

description of the dynamics in different areas in the FOV. Then we give a more detailed description of the dynamics in 3 regions-of-interest (ROI).

Isolated bright points show up in the *G*-band image in the regions of weakest overall magnetic field – such as in the lower right hand corner of Fig. 1. These seem to be passively advected with the general granular flow field in the intergranular lanes in the same way as previously described by e.g. Nisenson et al. (2003) and Berger et al. (1998). While we have not

conducted an exhaustive study of bright point lifetimes we find that bright points can be visible from some few minutes up to almost the entire length of the time series. We also find several examples of bright point merging, splitting and motions over several granular radii.

Figure 2 shows the Ca II H image cotemporal with the *G*-band image of Fig. 1. The Ca H filter is rather wide (0.3 nm) and centered slightly to the red side of the line-center. The filter intensity is therefore dominated by the inner wing intensity

rather than by the line-center intensity. The contribution function to intensity is rather broad with a mean formation height of 95–310 km in various quiet Sun features compared with –70–160 km in the *G*-band (Marthinussen 2004). Isolated magnetic flux points look much the same as in the *G*-band, and there is a good one to one correlation between isolated bright points seen in the *G*-band and in Ca H. However, as seen in Ca H the bright points are a little more smeared out, probably due to a combination of the wider contribution function for this passband and the longer exposure time (making this passband more susceptible to smearing by seeing).

A magnetogram made with the Ni I 676.8 nm line, formed 200 km above $\tau_{500} = 1$, is displayed in Fig. 3. In the magnetically quiet regions, isolated bright points show up as points without internal structure and with a field strength of roughly 1000 Mx cm^{-2} of either polarity.

In quiet regions, Dopplergrams such as Fig. 4 are dominated by the motions associated with the granular flow, i.e. upflow on the order of 500 m s^{-1} in the center of granules and downflows on the order of -500 m s^{-1} in the intergranular lanes; isolated magnetic bright points seem to be passively advected with the general granular flow and do not obviously perturb it.

Network-like areas with stronger average magnetic field are most easily recognized in the magnetogram and by bright emission in the Ca II H image, for example in the lower left corner and just right of the center in the bottom part of the FOV. The bright points in these areas are more numerous and interact more obviously with each other. Sometimes, bright points can be seen to coalesce into long thin strings in the intergranular lanes or conversely, strings are split into individual bright points. A detailed description of the evolution of such a string is given in the discussion of ROI 1 (Sect. 4.1). At other times the strings develop “knots” along their length. The strings are continuously kneaded and deformed by the granular motions, but the general pattern of bright strings remains much the same, often forming circular or hexagonal patterns outlining regions containing roughly 3–5 granules, for example as seen around the area $x = 35 \text{ Mm}$, $y = 20 \text{ Mm}$ in Fig. 1. Where the strings become thickest and more ribbon-like there are indications of internal structure: the ribbons have darker cores along their length as previously reported in Paper I. Ribbons form both along and at the vertices of intergranular lanes, extending several arms in starfish like shapes.

In Ca H (Fig. 2), the hexagonal patterns formed by the strings are sites of strong emission, outshining the background inverse granulation pattern. In regions where the strings are thickest and ribbon-like in the *G*-band, the Ca H signal is strong with the emission totally dominating the background.

Bright point strings, ribbons and the hexagonal patterns formed by them are also quite evident in the magnetogram shown in Fig. 3. The magnetic polarity is largely positive throughout the FOV, but there are large regions of negative polarity centered at $x = 3 \text{ Mm}$, $y = 27 \text{ Mm}$ and at $x = 42 \text{ Mm}$, $y = 41 \text{ Mm}$. The former is the site of vigorous activity and perhaps flux emergence.

Regions containing numerous ribbons are also evident in the Dopplergram, Fig. 4, where vertical velocities are obviously suppressed.

To the right of the central pore is an extended plage region, both ROI 2 and ROI 3 are chosen in this region. Here, the bright emission is concentrated in knotted ribbons with very few or no individual bright points visible. The ribbons themselves are arranged into a hexagonal pattern, with diameters on the order of a few granular cells, but the pattern is tighter than in the weaker field regions since the granulation in the plage region is markedly perturbed by the presence of the magnetic field, forming smaller than average granules. Again the pattern is, in detail, churned and kneaded by the granular flow but remains, on larger scales, much the same on the time scale of these observations. Where the density of ribbons is greatest they form roughly circular regions with corrugated edges resembling flowers (see also Paper I). The corrugated edges of the flowers, as well as the “knot”-like edges seen on the strings and ribbons (see ROI 2) closely resemble the structures predicted by Bünte (1993) and may therefore be the result of an interchange instability between the magnetic flux tubes or flux sheets concentrated in the intergranular lanes and the field free plasma. The central parts of flowers sometimes become dark, forming micropores. Likewise, micropores sometimes brighten into flowers. This behavior is described in more detail in ROI 3 (Sect. 4.3).

In Ca H the photospheric structures are much the same as those seen in the *G*-band, but there is an additional amorphous emission consisting of a large number of threads emanating from the entire plage region; this emission may be from chromospheric loops. At the upper right of the plage region many of these threads connect to the large negative polarity region that is seen up and to the right of the plage region, but there are also many threads that do not have an obvious termination point. Note that though the sunspot umbra, the penumbra and the large pore are dark also in Ca H, micropores are bright and indistinguishable in the general plage. On careful inspection we find similar threads spreading out from the pores and from the plage region, usually but not always directed towards regions of opposite polarity. These threadlike structures are quite thin, dynamic and short lived often being visible in only two or three consecutive frames. The width of these threads seems to be close to the diffraction limit and we only observe them in the best quality frames.

As imaged in Ca H, in the region surrounding the pore the reverse granulation pattern appears “washed out” with less contrast than in quiet regions. This difference in granulation is not obvious in the *G*-band and may be due to a large number of overlying chromospheric threads emanating from the pore.

The region to the left and slightly below the pore is a region of mixed polarity and of emerging magnetic flux. This is the only region in the FOV where positive and negative polarities are well mixed (see Fig. 3) and rapidly evolving: In general we find the background magnetic field to be fairly constant in spatial distribution during the 86 min this time series spans, but the region described here shows rapid motions, appearance and disappearance of magnetic signal.

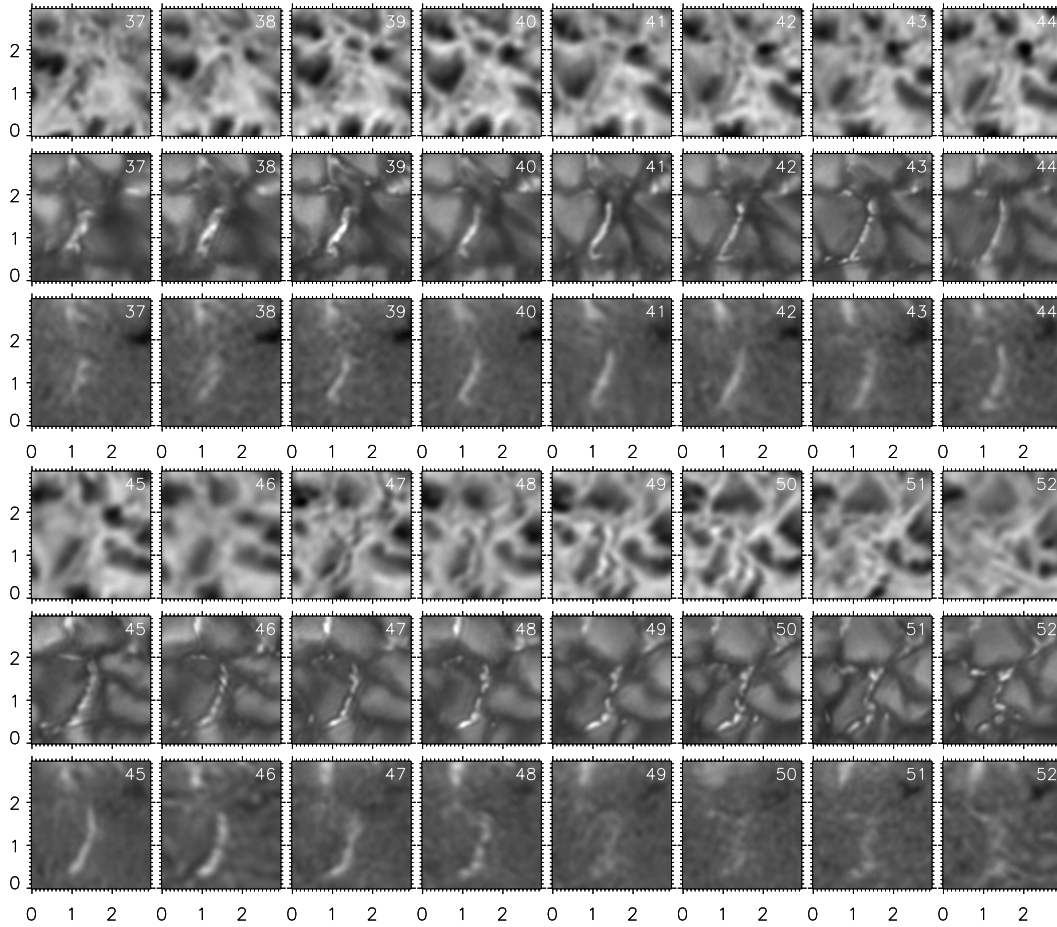


Fig. 5. Time evolution of ROI 1. Dopplergrams in top rows, *G*-band filtergrams in middle and magnetograms in bottom rows. Frame numbers in upper right corner. The cadence is 61.5 s. The range in Dopplershift is $[-827, 474]$ m s^{-1} with positive values corresponding to downward velocity and white in the figure. The range in magnetic flux density is $[-618, 665]$ Mx cm^{-2} . Spacing between large tickmarks is 1 Mm.

In the *G*-band the dynamics are characterized by rapidly moving individual bright points, strings, and ribbons, and by perturbed – “stretched out” – granulation displaying large horizontal velocities. In particular, a flux emergence event is seen by two individual bright points moving rapidly away from each other, accompanied by a “wake” in the pattern of granulation between them. Observed in the magnetograms the event is seen as two regions of opposite polarity moving apart.

This region is also the region of greatest emission in the Ca H filter. We find that the emerging flux bright points and plage show enhanced brightness and, again, that thin thread-like structures typically stretch between the regions of opposite polarity. Any single thread is difficult to follow for more than two to three frames and the connectivity between any two given regions, as outlined by the dynamic threads, seems to change quite rapidly with time in this region.

When viewed in Doppler velocity we find a signature of flux emergence characterized by a rapid initially circular upflow between the sites of opposite magnetic polarity, this upflowing region is, like the granulation itself, stretched out by the movement of the magnetic poles, gradually becoming weaker and fading into insignificance after 10–12 min. In addition, each magnetic pole seems to have associated with it a strong

and concentrated downflow that follows along with the photospheric field motion.

Now we describe the dynamical evolution in the ROIs in more detail.

4.1. ROI 1: Flux sheet

Figure 5 shows the temporal evolution in ROI 1 in the 934 s time interval from UT 09:06:17 to 09:21:51. The figures show magnetic flux that is first advected to form a thin sheet. The sheet fragments after a certain time into a number of bright points that are subsequently dispersed by the granular flow field.

In the Dopplergrams shown in the top rows the granular flow pattern is much as expected; upflows (dark in the figure) are prevalent inside granules while downflows (bright) are concentrated in the intergranular lanes. In the flux sheet itself we find a weak *upflow*. The upflow velocity is largest just before the formation of the sheet, about 250 m s^{-1} in frame 37 and reduces to about 100 m s^{-1} and lower at later stages. The intergranular downflow is concentrated to the immediate vicinity of the flux sheet and is about 300 m s^{-1} . The magnetic flux concentrations seen as bright features in the bottom row

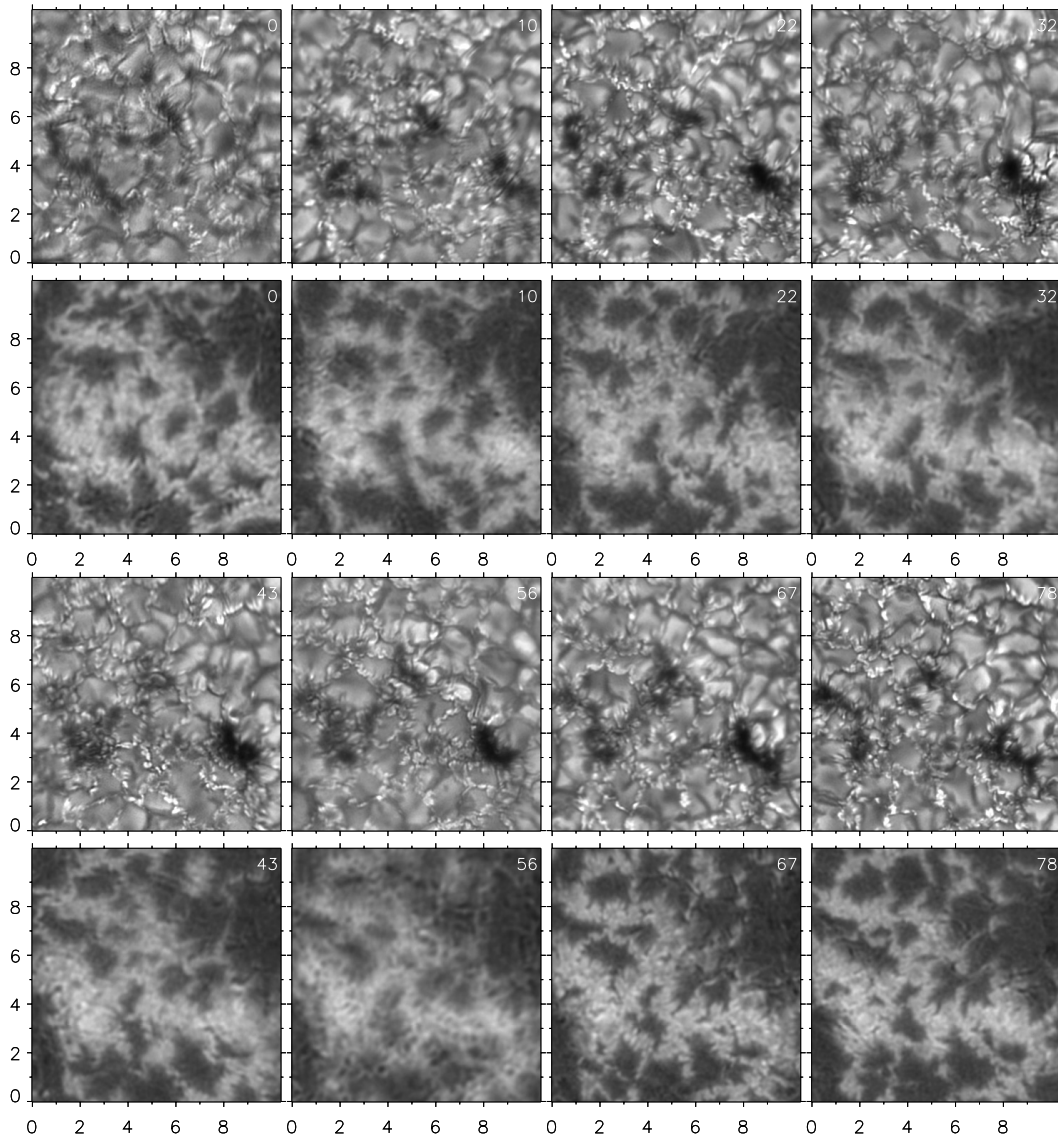


Fig. 6. Time evolution of ROI 2. *G*-band 430.5 nm filtergrams in top rows, magnetograms in bottom. Frame numbers in upper right corner. Time between two consecutive frame numbers is 61.5 s giving an average time of 685 s between the images shown. The range in magnetic flux density is $[-229, 1312]$ Mx cm^{-2} . Spacing between large tickmarks is 1 Mm.

magnetograms, with flux density up to 650 Mx cm^{-2} , correspond to bright areas in the *G*-band filtergrams and to weak upflows in the Dopplergrams.

When the sheet fragments, possibly due to flute-instability (Bunte 1993), fingers of stronger downflow creep into the areas the sheet previously occupied (e.g. frames 47–48).

It is unlikely that the extended structure we see in the first 5 frames is in fact composed of separated bright points of sizes like in the last frames but smeared by seeing. In fact, the resolution achieved in the first frames is better than later in the sequence, as indicated by contrast measurements on a larger area than the region shown in Fig. 5.

4.2. ROI 2: Plage region

Figure 6 shows the temporal evolution in ROI 2 in the 4855 s time interval from UT 08:27:54 to 09:48:49. This ROI has been

chosen to demonstrate the appearance and disappearance of micro-pores.

This region is part of an extended plage region and is mostly covered with magnetic structures of almost exclusively positive polarity, up to a magnetic flux density of 1300 Mx cm^{-2} . Close to the right edge of the figure there are also some negative polarity regions as seen in the magnetograms (bottom rows). The *G*-band pattern shown in the top rows is complex, with ribbon-like structures of knotted appearance and a number of darker regions resembling small pores or micro-pores.

Consider now the time evolution of the micro-pore in the lower right hand of the figure. It is most pronounced in frame 43, while being absent at the beginning of the time-series. Towards the end of the time series it is on the verge of vanishing again. The other micro-pores also come and go. Such features seem to evolve continuously between ribbon like

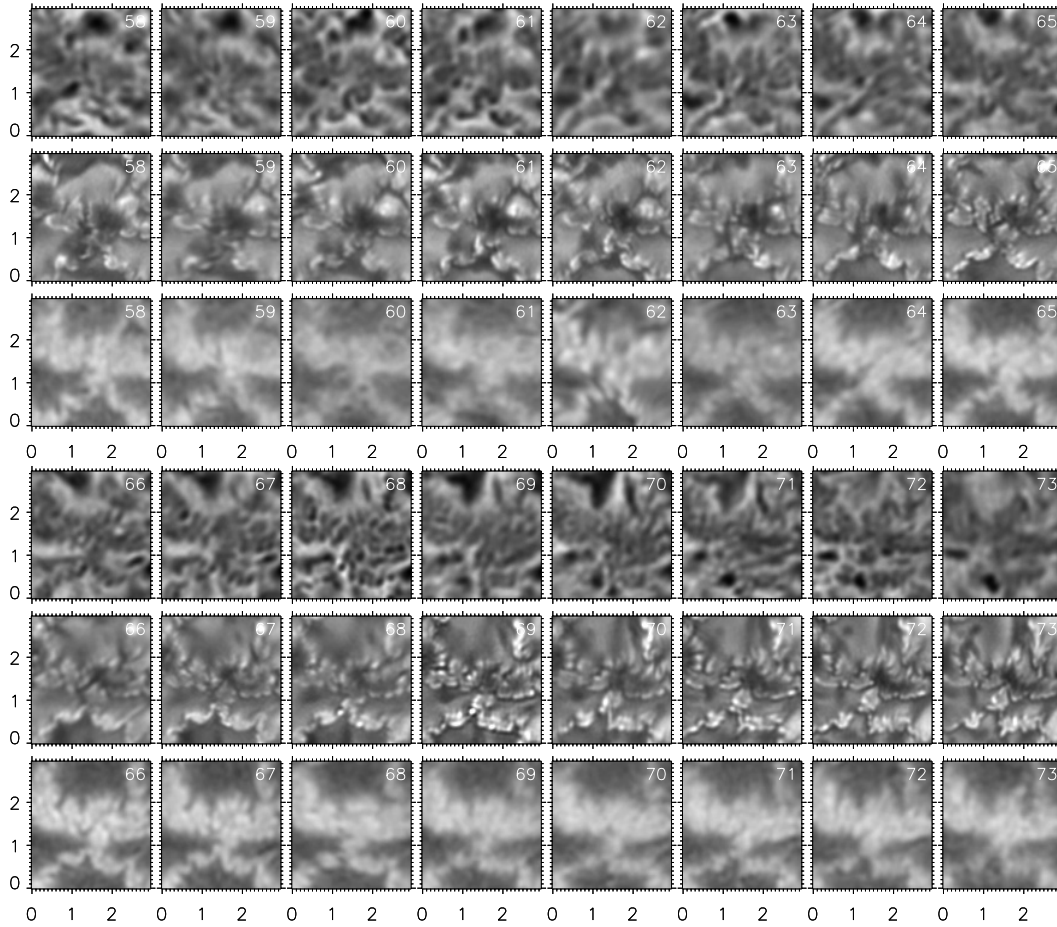


Fig. 7. Time evolution of ROI 3. Dopplergrams in top rows, *G*-band filtergrams in middle and magnetograms in bottom rows. Frame numbers in upper right corner. The cadence is 61.5 s. The range in Dopplershift is $[-474, 514]$ m s^{-1} with positive values corresponding to downward velocity and white in the figure. The range in magnetic flux density is $[-65, 1076]$ Mx cm^{-2} . Spacing between large tickmarks is 1 Mm.

structures, structures that resemble the “flowers” of Paper I, and micro-pores.

In general, the *G*-band shows the brightest features where there is strong magnetic field with small lateral extent, shows a knotted, ribbon-like structure when the magnetic filling factor is larger, and a micro-pore for the largest in extent magnetic regions. The appearance at any given position varies as the magnetic field evolves in strength and horizontal extent as a result of photospheric motions.

4.3. ROI 3: Ribbon

Figure 7 shows the temporal evolution in ROI 3 (a subfield of ROI 2) in the 934 s time interval from UT 09:28:04 to 09:43:38. As in ROI 1 the top row shows Dopplergrams, the middle rows show *G*-band intensities, while in the bottom row magnetograms are shown. This ROI features small-scale details of a strong field, plage region as well as another look at the disappearance and appearance of a micro-pore.

There is no normal granulation pattern within this ROI. Just above the middle of the field there is a wide band of magnetic flux crossing the region. Below the middle there is an arc of magnetic flux that is quite thin, down to 100 km thickness. The plasma is typically at rest in the magnetic flux

concentrations with some localized areas containing weak up-flows. The velocity varies around 0 m s^{-1} with a maximum upflow of 150 m s^{-1} . The intergranular downdrafts are concentrated in narrow sheets and located right at the edge of the magnetic flux concentrations and reach up to 360 m s^{-1} . Examples of strong gradients with 150 m s^{-1} upflow sites next to intergranular downdrafts are at $x = 1 \text{ Mm}$, $y = 0.5 \text{ Mm}$ on frame 61 and $x = 1.3 \text{ Mm}$, $y = 0.8 \text{ Mm}$ on frame 68. The wide band of strong magnetic flux just above the middle shows time varying appearance in the *G*-band filtergrams, basically with a ribbon-like structure with dark central lane and knotted brighter edges. These brighter edges sometimes meet to form small flower-like structures (e.g. in frames 69 and 72), sometimes they are wider and look like micro-pores (e.g. first half of time-series). The forms continuously change with the life-time of the knotted structures on the order of 3–5 min.

5. Discussion and conclusions

Solar convective motions continuously churn the outer solar atmosphere. Hot, high entropy gas is brought up to the photosphere where the excess energy is radiated away. Cool low entropy material descends into the depths in steadily narrower lanes and plumes as described by Stein & Nordlund (1998).

The result of these motions is, of course, the granular pattern observed on the solar surface. Along with rising and falling plasma, magnetic field is carried with the flow forming various structures. Some of these structures are quite small and have only become evident at angular resolution better than 0'.3 or so.

We have in this paper discussed such structures in the form of bright points, strings, ribbons, micro-pores and pores. In order for these structures to become visible at all they must attain field strengths of sufficient amplitude to perturb the plasma they are embedded in. Thus, we expect that there also exists a whole hierarchy of magnetic structures which have not yet attained such a critical field strength. What is the source of this field? One possible scenario is that it is brought up in granules at field strengths too low to leave an observational signature in intensity. Granular flow then carries this field to the intergranular lanes and ultimately to the intergranular intersections where it may become compressed and strong enough to make the field visible, i.e. on the order of 1500 Gauss for a photospheric pressure of 10^5 dyn/cm². This is then the reason bright points always seem to appear in intergranular intersections. This behavior has been reported by a number of observers, see e.g., van Ballegoijen et al. (1998), Nisenson et al. (2003).

The larger magnetic filling factor in the plage region gives rise to flowers, ribbon-like structures and micro-pores. These are characterized by a knotted, brighter edge and lower intensities in the interior. There is a continuous transition between these tracers of strong magnetic field. This is consistent with magneto-convection simulations (Carlsson et al. 2004); The increased brightness in magnetic elements is due to their lower density compared with the surrounding intergranular medium. One thus sees deeper layers where the temperature is higher. At a given geometric height, the magnetic elements are cooler than the surrounding medium because the magnetic fields prevent convective energy transport from deeper layers. At the edges of the flux concentrations the plasma is radiatively heated by the surrounding hotter, non-magnetic plasma. At some strength the flux sheets become unstable to a fluting instability and the edges buckle as we have shown in this paper.

The general behavior of the temporal evolution of strong-field areas and in particular of the examples discussed in this paper; the merging and splitting of flux sheets and the continuous transition between ribbons and micropores, are difficult to reconcile with models that regard extended magnetic structures as being composed of discrete fluxtubes that keep their identity over a long period of time. It is more appropriate to characterize the temporal behavior of the magnetic field in these areas as fluid-like. This "magnetic fluid" is in continuous interaction with the field-free plasma, sometimes forming extended structures like micro-pores, sometimes being concentrated into ribbons, flowers or sheets. Sheets may fragment into flux-tube-like structures. Such fluid-like behavior of magnetic flux is also forcefully demonstrated in recent magneto-hydrodynamic simulations (see e.g., Carlsson et al. 2004; Vögler et al. 2005).

We find that the plasma is basically at rest in the ribbons with small fluctuations on the order of 100 m s⁻¹ in either direction. Sometimes, upflows are found of about 150 m s⁻¹ within localized concentrations in the ribbons and also in smaller-scale magnetic features such as the flux sheet found in ROI 1.

Stronger downflows are found in narrow sheets at the edges of ribbons and in the immediate vicinity of bright points and flux sheets. The finding of such narrow downflow sites just outside magnetic field concentrations was earlier reported by Rimmele (2004) and Paper I. The latter two studies only find downflows associated with magnetic field concentrations. Rimmele (2004) finds downflows of a few hundred m s⁻¹ in the deep photosphere but only weak velocities in the higher photospheric layers. The Ni I line we use for our study is also formed in the higher photospheric layers and given the errors in the Dopplergrams and calibrations, our finding of weak upflows in magnetic structures is not in direct conflict. For the weak downflows that were consistently found in all magnetic structures in Paper I, we point out that these Doppler measurements in the magnetic areas were biased since only RCP exposures were used for the Ni I Dopplergram. In any case, the velocity amplitude is typically low, about 150 m s⁻¹, so it can be concluded that there is only little plasma motion in magnetic structures.

Acknowledgements. This research was supported by the European Community's Human Potential Programme through the European Solar Magnetism Network (ESMN, contract HPRN-CT-2002-00313), from The Research Council of Norway through grant 146467/420 and through a grant of computing time from the Programme for Supercomputing, by NASA grant NAS5-38099 (TRACE), and Lockheed Martin internal research and development funds. The Swedish 1-m Solar Telescope is operated on the island of La Palma by the Institute for Solar Physics of the Royal Swedish Academy of Sciences in the Spanish Observatorio del Roque de los Muchachos of the Instituto de Astrofísica de Canarias. We thank the staff of the SST including Göran Scharmer, Peter Dettori, Rolf Keiver, and Göran Hosinsky for assistance in all aspects of the observations. MDI data was obtained from the Stanford Oscillations Investigation website; SOHO is a project of international cooperation between ESA and NASA.

References

- Berger, T., Rouppe van der Voort, L., Löfdahl, M., et al. 2004, A&A, 428, 613 (Paper I)
- Berger, T. E., Löfdahl, M. G., Shine, R. S., & Title, A. M. 1998, ApJ, 495, 973
- Berger, T. E., Schrijver, C. J., Shine, R. A., et al. 1995, ApJ, 454, 531
- Berger, T. E., & Title, A. M. 1996, ApJ, 463, 365
- Bovelet, B., & Wiehr, E. 2003, A&A, 412, 249
- Büntje, M. 1993, A&A, 276, 236
- Carlsson, M., Stein, R. F., Nordlund, Å., & Scharmer, G. B. 2004, ApJ, 610, L137
- Dunn, R. B., & Zirker, J. B. 1973, Sol. Phys., 33, 281
- Kiselman, D., Rutten, R. J., & Plez, B. 2001, in Proc. IAU Symp. 203, ed. P. Brekke, B. Fleck, & J. B. Gurman, 287
- Löfdahl, M. G. 2002, in Image Reconstruction from Incomplete Data II, ed. Bones, Fiddy, & Millane, Proc. SPIE 4792, 146
- Marthinussen, E. 2004, Imaging of the solar photosphere: Simulation, observation and methods of interpretation, Norway: MSc Thesis, Institute of Theoretical Astrophysics, University of Oslo
- Muller, R. 1983, Sol. Phys., 85, 113
- Muller, R., Roudier, T., Vigneau, J., & Auffret, H. 1994, A&A, 283, 232
- Nisenson, P., van Ballegoijen, A. A., de Wijn, A. G., & Sütterlin, P. 2003, ApJ, 587, 458

- Rimmele, T. R. 2004, *ApJ*, 604, 906
- Rutten, R. J., Kiselman, D., Rouppe van der Voort, L., & Plez, B. 2001, in *Advanced Solar Polarimetry – Theory, Observation, and Instrumentation*, ed. M. Sigwarth, ASP Conf. Ser., 236, 445
- Sánchez Almeida, J., Asensio Ramos, A., Trujillo Bueno, J., & Cernicharo, J. 2001, *ApJ*, 555, 978
- Schüssler, M., Shelyag, S., Berdyugina, S., Vögler, A., & Solanki, S. K. 2003, *ApJ*, 597, L173
- Scharmer, G. B., Bjelksjö, K., Korhonen, T. K., Lindberg, B., & Petterson, B. 2003a, in *Innovative Telescopes and Instrumentation for Solar Astrophysics*, ed. L. K. Stephen, & V. A. Sergey, Proc. SPIE, 4853, 341
- Scharmer, G. B., Dettori, P. M., Löfdahl, M. G., & Shand, M. 2003b, in *Innovative Telescopes and Instrumentation for Solar Astrophysics*, ed. S. L. Keil Sergey, & V. Avakyan, Proc. SPIE, 4853, 370
- Scharmer, G. B., Gudiksen, B. V., Kiselman, D., Löfdahl, M. G., & Rouppe van der Voort, L. H. M. 2002, *Nature*, 420, 151
- Scharmer, G. B., Kiselman, D., Löfdahl, M. G., & Rouppe van der Voort, L. H. M. 2003c, in *Proc. Third International Workshop on Solar Polarization*, ASP Conf. Ser., 307
- Shelyag, S., Schüssler, M., Solanki, S. K., Berdyugina, S. V., & Vögler, A. 2004, *A&A*, 427, 335
- Stein, R. F., & Nordlund, A. 1998, *ApJ*, 499, 914
- Steiner, O., Hauschildt, P. H., & Bruls, J. 2001, *A&A*, 372, L13
- Title, A. M., & Rosenberg, W. 1981, *Optical Engineering*, 20, 815
- Title, A. M., Tarbell, T. D., Topka, K. P., et al. 1989, *ApJ*, 336, 475
- Title, A. M., Topka, K. P., Tarbell, T. D., et al. 1992, *ApJ*, 393, 782
- Uitenbroek, H. 2003, in *Current Theoretical Models and Future High Resolution Solar Observations: Preparing for ATST*, ed. A. A. Pevtsov, & H. Uitenbroek, ASP Conf. Ser., 286, 403
- Vögler, A., Shelyag, S., Schüssler, M., et al. 2005, *A&A*, 429, 335
- van Ballegoijen, A. A., Nisenson, P., Noyes, R. W., et al. 1998, *ApJ*, 509, 435